Applied Thermal Engineering 99 (2016) 133–146

Contents lists available at ScienceDirect

Applied Thermal Engineering

journal homepage: www.elsevier.com/locate/apthermeng

Research Paper

Numerical and experimental investigation of a counter-current two-phase thermosyphon with cascading pools

Marc Schreiber [a], Wessel W. Wits [a,*], Gert Jan te Riele [b]

[a] Faculty of Engineering Technology, University of Twente, P.O. Box 217, 7500 AE Enschede, The Netherlands
[b] Thales Nederland B.V., P.O. Box 42, 7550 GD Hengelo, The Netherlands

HIGHLIGHTS

- An innovative counter-current two-phase thermosyphon is presented.
- The thermosyphon features multiple pools cascaded along the evaporator section.
- Liquid accumulates in the pools until they overflow to spread the working fluid.
- A numerical control volume model and experimental validation are discussed.
- The paper includes an interactive 3D model and a video of the working prototype.

ARTICLE INFO

Article history:
Received 28 September 2015
Accepted 22 December 2015
Available online 19 January 2016

Keywords:
Closed two-phase thermosyphon
Multiple evaporator sections
Control volume approach
Boiling heat transfer

ABSTRACT

An innovative design of a counter-current two-phase thermosyphon is investigated for the in-plane cooling of flat product structures. The thermosyphon features multiple pools staggered along the entire evaporator section, in which liquid flowing toward the bottom of the thermosyphon can be stored. The pools are used to cascade the working fluid to the evaporator end cap. Liquid accumulates in the pools until they overflow, thereby spreading the working fluid across the entire evaporator length rather than creating one liquid pool at the bottom end cap. Multiple of such thermosyphons operating in parallel can be used for low-gradient planar cooling of vertically oriented surfaces. A numerical model using a control volume approach is developed to predict and to validate the experimental results of this innovative design. The main advantages of the control volume approach are the adaptability of the entire model and the fast computational speed in comparison to elaborate fluid dynamics models. Empirical correlations are used for the modeling of the heat transfer coefficients and friction factors of the counter-current flow. A proof of principle is given by observing a prototype that was milled into a copper bar. Next to logging temperature measurements, the prototype had a glass top plate to visually record the working fluid behavior. The model presented is well suitable for the early stages of thermosyphon design studies and for the impact evaluation of design changes.

1. Introduction

Heat transfer in cooling applications generally requires a low thermal resistance, which can be challenging using conventional forced convection methods. The physical phenomenon of phase transition and the ability to store energy as latent heat can be utilized to meet these low thermal resistance performance criteria. Thermosyphons are among other devices capable of transferring heat utilizing phase transition as the working principle. A common counter-current two-phase thermosyphon (alt. thermosiphon), as shown in Fig. 1a, is a closed tube with a working fluid inside. In this figure heat is supplied at the bottom of the thermosyphon where a pool of working fluid resides. The working fluid is circulating inside the tube due to phase changes caused by the heat transfer at the bottom (evaporator section) and at the top (condenser section). In the condenser section vaporized working fluid condenses as heat is extracted from the system and forms a liquid film along the thermosyphon wall. Gravitational forces (or centrifugal forces) are used to transport the condensed liquid back toward the evaporator section along the wall of the thermosyphon [1].

Because of their relative simple structure and low cost, thermosyphons are widely used as heat transfer devices (e.g. thermal management systems, heat exchangers and reboiling applications) in various applications [2]. The performance of the thermosyphon depends on the thermophysical properties of the working fluid, the fill ratio, the geometrical shape, the inclination angle and the operating conditions [3,4]. Various limitations regarding the working principle exist that can lead to rupturing or

* Corresponding author. Tel.: +31 (0)53 489 2266.
E-mail address: w.w.wits@utwente.nl (W.W. Wits).

http://dx.doi.org/10.1016/j.applthermaleng.2015.12.095
1359-4311/

severe overheating of the thermosyphon. A major benefit compared to other heat transport devices is that no external power supply is needed for the migration of the working fluid other than a present heat source and gravitational field (or centrifugal forces). Liquid can also be transported using a wick structure, making it possible to function in any orientation. Such devices are commonly known as heat pipes.

1.1. Introduction to the new design

This paper presents an innovative design for a counter-current two-phase closed thermosyphon with cascading pools, as shown in Fig. 1b. This design focuses, in contrast to the classical thermosyphon design, on a relative long evaporator section in comparison to the adiabatic and condenser sections. The goal is to minimize the temperature gradient and temperature fluctuation along the entire length of the evaporator. This is done by having multiple cascading pools along the entire length of the thermosyphon's evaporator section. This enables the cooling of large planar surfaces in which space is a design constraint and heat needs to be dissipated effectively at an affordable cost. The design is further discussed in Section 2. An experimental apparatus was built based on a numerical model using a control volume approach. The experimental apparatus was used to gather both thermal measurement data and visual operations of the two-phase working principle to review the working principle and the performance. The numerical method focuses on good overall prediction, adaptability and computation speed. A comparison between the model and the experimental data is made and discussions about the findings are reported.

1.2. Literature review

The first tube with a two-phase cycle, called the Perkins tube, was patented by Jacob Perkins in 1836 [5]. Early research on counter-current two-phase closed thermosyphons was performed by Cohen and Bayley [6]. Most of the early research focused on specific phenomena, such as the heat transfer behavior in various sections and operation limitations [1]. The theoretical results were often compared with experimental data and empirical correlations were reported. Recent research surrounding this field seems to be more concentrated on the use of elaborate numerical optimization models [4,7], with the focus on accurate results.

1.2.1. Thermosyphon limitations

The operating limitations for thermosyphons describe the boundaries wherein the device should operate as designed. An important limitation is the flooding limitation. Shear on the liquid–vapor interface causes liquid to return to the condenser section when the shear forces are greater than the surface tension forces. Contributions for determining the flooding limitation were made by various researchers [8–12]. Other researchers contributed to the determination of correlations for the dry-out limitation [6,13,14]. Dry-out is reached when the amount of working fluid is small in comparison to the supplied heat, resulting in the entire vaporization of the liquid puddle at the bottom evaporator section. Finally, also the boiling limitation has been researched extensively [15,16]. This limit is encountered when the boiling regime changes from nucleate to film boiling, creating an insulating vapor layer between the wall and the liquid, causing the evaporator wall temperature to rise unacceptably.

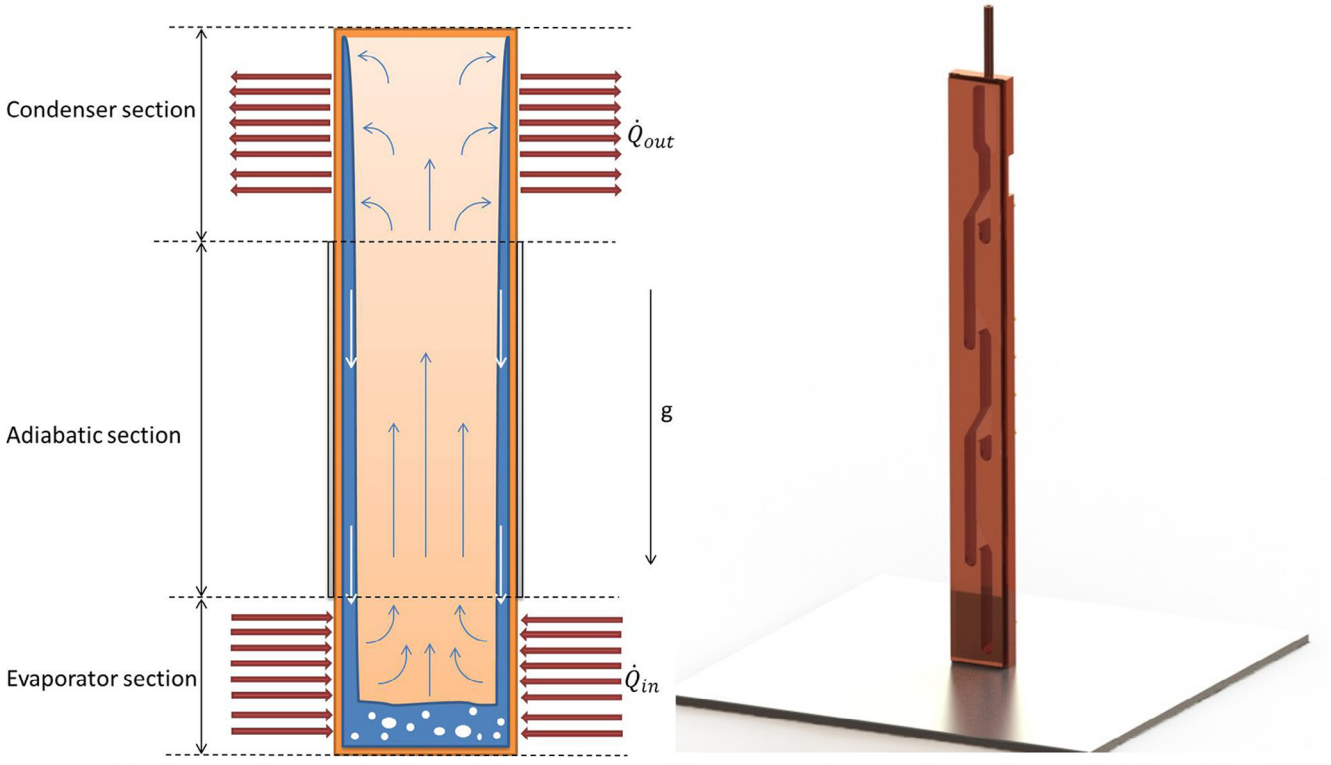

(a) schematic drawing of a classical design (b) innovative design with cascading pools (3D model in PDF)

Fig. 1. Counter-current two-phase closed thermosyphon design.

1.2.2. Thermosyphon boiling regime

The heat transfer mechanism and the fill ratio greatly influence the performance of the thermosyphon. Studies concerning the optimal fill ratio were carried out by Imura et al. [17] and Park et al. [18]. Convection boiling and evaporation are dominating at low fill ratios. For this study, in which a long evaporator section is present, it is plausible that with a low fill ratio the liquid film breaks down into rivulets. If the liquid pool is not covering the entire length of the evaporator, a decrease in heat transfer and consequently a rise in the wall temperature of the evaporator can occur [17]. Nucleate pool boiling is likely to occur at higher fill ratios and heat fluxes. A further increase of the fill ratio leads to geyser boiling [19]. This is especially dominant for working fluids with a high surface tension, such as water. A drop in thermal performance and undesired fluctuations in evaporator temperature are the result. The temperature fluctuations are related to energy storage in the liquid and its rapid release during vapor nucleation [20]. Cavitation damage due to geyser boiling can occur if the liquid that bursts away from the pool strikes the condenser end cap.

1.2.3. Heat transfer coefficients

Many heat transfer coefficients to model evaporator behavior during various boiling regimes are proposed in the literature [19,21,22]. The heat transfer coefficient from Nusselt film theory [23] and similar correlations [22,24] can be used for modeling heat transfer in the condenser region. Minor differences between the correlations for film condensation are based on the assumptions regarding these expressions, e.g. the flow regimes. Nusselt film theory was incorporated successfully by Streltsov [13] in his analytical analysis of a thermosyphon assuming laminar flow. Rohsenow's correlation [22] differs from Nusselt's correlation by taking into account the effect of sub-cooling of the condensate film. Kutateladze [24] proposed a simple relation to determine the heat transfer coefficient in a wavy-laminar flow on vertical planes. The Kutateladze equation typically predicts an even higher value of the heat transfer coefficient for typical values of the Reynolds number for a wavy-laminar flow.

1.2.4. Control volume approach

Designing on a higher system level or generating many design variants during the concept phase could benefit from numerical analyses, e.g. finite element method, finite difference method, variational approach and finite volume method. Investing time in running a detailed numerical model that needs to be adapted frequently can be an undesired solution in such a case. In order to meet this time management requirement, computational time can be reduced by using a time effective model. The numerical approach adopted in this paper is based on earlier work of Vincent and Kok [3] and recent work of Wits and Kok [25]. These methods are based on a lumped one-dimensional finite volume approach that solves the mass, momentum and energy conversation equations for a number of control volumes. Depending on the number of elements the computation time is considerably lower than with an extensive computational fluid dynamics analysis. The impact of adaptations to the thermosyphon design can therefore be evaluated faster during the design process at the expense of accuracy of the results. Wall temperatures and friction coefficients still need to be determined using empirical relations. These are adopted from the literature described in previous sections.

2. The proposed innovative design

Integrating a two-phase closed thermosyphon into a product may require changes to the basic structure. In recent years, studies on flattened two-phase closed thermosyphons were carried out by Srimuang et al. [26] and Amatachaya and Srimuang [27]. Experiments on a flat horizontal disk-shaped thermosyphon were carried out by Zhang et al. [28] in 2008. Lee et al. [29] proposed an alternative design using a double evaporator in 2009, showing some similarities with the working principle of the design proposal of this paper. The proposed design of this paper, as shown in Fig. 1b, is to be integrated into large planar surfaces in which the thermosyphon's profile is milled into the planar structure. Multiple milled thermosyphons can be incorporated in parallel into one plate of material, creating a planer cooling surface with multiple thermosyphons. The condenser sections of the thermosyphons are positioned at the upper end, where typically a secondary heat exchanger is placed to further extract the heat.

2.1. Principle of cascading pools

In order to minimize the effects of fill ratio and boiling mechanism on the thermal performance, a pattern of pools along the thermosyphon length is designed. Fig. 2 shows the dimensions for a design with four additional pools above the bottom pool. The pools create heat sinks in which the working fluid accumulates and nucleate boiling can be initiated. Liquid returning from the condenser section flows toward the evaporator section. The liquid accumulates in a pool until it overflows. Nucleate boiling and sudden bursts in the pools will also help the liquid to flow downward. Liquid that overflows is able to flow to the pools below, creating a cascading effect. Fig. 3a illustrates this process from left to right for one pool.

2.2. Pool design

In order to reduce shear stress on the liquid film, the vapor passage is kept as uniform as possible, having only slightly curved bends. Not all liquid returning from the condenser will accumulate in the top pool, as surface tension forces and adhesion guide the liquid along the thermosyphon wall toward lower situated pools. The pool is U-shaped for production purposes; a prototype pool and its vapor passage, milled into a bar of copper, are shown in Fig. 3b. The cascading pools have a depth of 12 mm from top to bottom and can contain approximately 0.7 ml. In the proposed design, five liquid pools, including the bottom end cap, are present along the entire thermosyphon's evaporator section. The chosen liquid fill ratio lies between 15% and 19% of the total volume of the thermosyphon during operation. The depth of the pools and the liquid fill ratio are optimized using the numerical model discussed in Section 3.4.

2.3. Overall thermosyphon design

The cross section of the thermosyphon is of rectangular shape, which is milled into a $380 \times 40 \times 10\ mm^3$ bar of Electrolytic-Tough-Pitch (ETP) copper. ETP copper was chosen as the base material for its high thermal conductivity. The thermosyphon has a depth of 8 mm. The heated area of the copper profile has a length of 300 mm. The cooled condenser section has a length of 50 mm. The adiabatic section has a length of 30 mm. Other relevant dimensions are presented in Fig. 2 as well. In order to observe the behavior of the working fluid, a glass screen is bonded to the front. The glass cover provides the advantage of visualizing and recording the liquid behavior in the thermosyphon. Note that the glass screen influences the heat transfer characteristics. The glass material was chosen because of its low gas diffusivity and clear transparency. The condenser section is wider than the evaporator section and has a volume of $43 \times 16 \times 8\ mm^3$. A copper tube is soldered onto the top of the thermosyphon to connect it to a

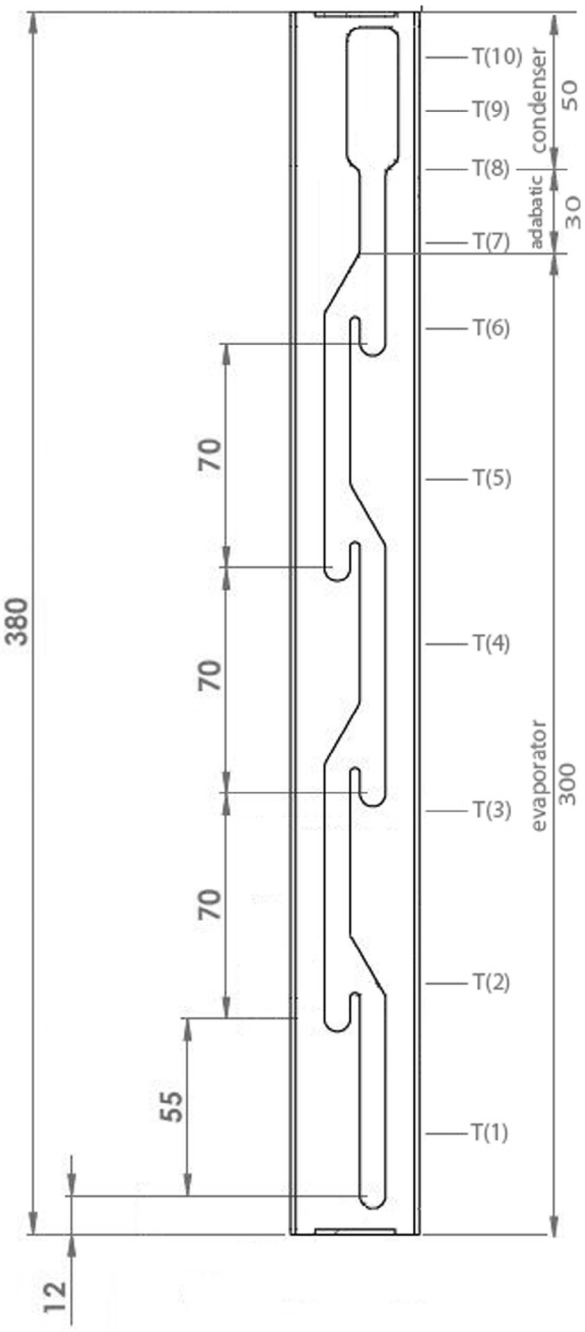

Fig. 2. Typical dimensions for a thermosyphon with cascading pools.

filling rig. This filling rig is used to evacuate non-condensible gases and adjust the fill ratio.

3. Modeling approach

The use of a transient model during the design process of this thermosyphon was needed to validate the results and to make various design decisions regarding the structure of the experimental model. The transient model makes use of empirical relations and finite volume elements containing both liquid and vapor of the same substance. The upcoming sections describe this model in further detail, focusing on the numerical model, the use of empirical relations and the boundary conditions, respectively.

3.1. Numerical modeling

The variables used in the upcoming sections are related to Fig. 4, which shows finite volume element i and its neighbors $i-1$ and $i+1$. In this figure heat $\dot{Q}_i$ is supplied to the element, therefore the element acts as an evaporator. Liquid flows from right to left assisted by gravity and the vapor flows from left to right. The geometric relations between entities are listed in Table 1. In the transient model properties like liquid height and vapor cross sectional area are modeled after the basic finite volume element depicted in Fig. 5a. Fig. 5b shows a similar element however with a cascading pool. The volume associated with a cascade pool V_{pool} represents the liquid buffer an element can contain before the liquid 'overflows'. The excess liquid flows out of the control element toward it neighboring element $i-1$.

3.1.1. Conservation of mass

The conservation of mass states that the time rate of change of mass inside the control volume is accounted for by the net mass flow across the boundary of the system [30,31]:

$$\frac{d}{dt}\int_{V_{j(t)}}\rho_j dV_i + \int_{S_{j(t)}}\rho_j(\mathbf{u}_{j,rel}\cdot\boldsymbol{n})dS_j = 0 \quad \forall j = l, v \tag{1}$$

The mass of the substance inside an element is independent of the state of the substance, therefore the separate states can be taken together. By lumping the masses of the two separated states in a 1D element and assuming that the mass of one state can only flow across two boundaries surfaces, Eq. (1) can be rewritten in a more usable form (Eq. 2). Flows in these equations correspond with the directions shown in Fig. 4.

$$\frac{d}{dt}\left(\rho_{l,i}V_{l,i} + \underbrace{\rho_{v,i}V_{v,i}}_{=0}\right) = \rho_{v,i-1}S_{v,i-1}\bar{u}_{v,i-1} - \rho_{v,i}S_{v,i}\bar{u}_{v,i} + \rho_{l,i+1}S_{l,i+1}\bar{u}_{l,i+1} - \rho_{l,i}S_{l,i}\bar{u}_{l,i} \tag{2}$$

The time rate of change of the vapor volume is negligible as the density $\rho_v \ll \rho_l$ and is left out of this equation because of the low impact. The properties of the substance of the inflow are determined by the neighboring finite volume properties and boundary conditions are taken from where the flow originates. The properties of the liquid and vapor are taken constant throughout the entire finite volume. The surface of the liquid S_l is related to the liquid height of the film.

The mass flow across the liquid–vapor interface $\dot{m}_{lv,i}$ can be determined from the mass conservation equation of the liquid volume within the control element (Eq. 3). This mass flow is needed for determining the energy associated with the latent heat in the energy conversation equation.

$$\frac{d}{dt}(\rho_{l,i}V_{l,i}) = \rho_{l,i+1}S_{l,i+1}\bar{u}_{l,i+1} - \rho_{l,i}S_{l,i}\bar{u}_{l,i} - \dot{m}_{lv,i} \tag{3}$$

3.1.2. Finite elements regarding cascading pools

The conservation equations regarding the cascading pools are dependent on the amount of liquid buffer the element contains. This means that the mass flow surface of the liquid outflow S_l becomes a case-based function of the liquid buffer V_{pool} and the total liquid volume V_l (Eq. 4). Using this condition, the liquid can accumulate in the thermosyphon before outflow occurs.

$$S_l = \begin{cases} \dfrac{V_l - V_{pool}}{L} & V_l - V_{pool} > 0 \\ 0 & V_l - V_{pool} \le 0 \end{cases} \tag{4}$$

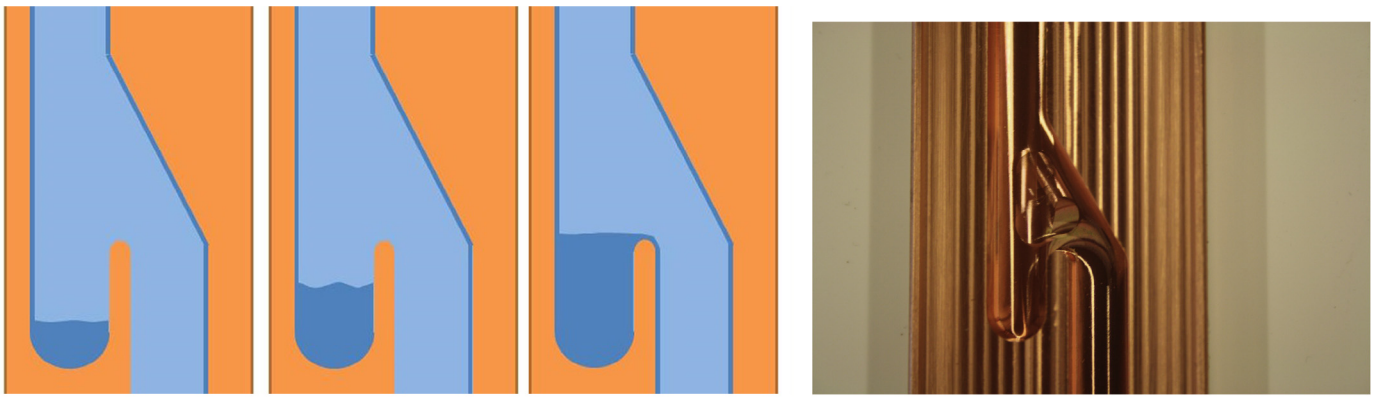

(a) schematic of overflowing pool behavior (b) prototype liquid pool and vapor passage

Fig. 3. Principle and design of a cascading pool.

3.1.3. Conservation of energy

The increase in energy over time in a control volume equals the rate of accumulation of energy inside the volume and the change of energy flowing across the control volume's boundaries. The heat rate inside the control volume is the integral of all heat fluxes of the control volume's boundaries. Heat generation is not considered to occur inside the volume [30,31]. The work done on a volume consists of the work done by the surface forces (pressure p and viscous shear stress $\boldsymbol{\tau}$ at the boundaries) and the work done by the volume forces. However, in a thermosyphon the energy associated with the work is negligible compared to the energy associated with the heat: $\frac{d}{dt}Q \gg \frac{d}{dt}W$. Therefore the work done by the body forces and the viscous forces is neglected in the energy conservation equation, leading to Eq. (5):

$$\frac{d}{dt}\int_V \rho E dV + \int_S \rho E(\boldsymbol{u}\cdot\boldsymbol{n})dS + \int_S q\boldsymbol{n}dS + \int_S p(\boldsymbol{u}\cdot\boldsymbol{n})dS = 0 \tag{5}$$

The work done by the pressure forces is not neglected, as it is needed for the conversion of the specific heat at constant volume c_V to the specific heat at constant pressure c_p, using the definition of specific enthalpy. It is assumed that the liquid flow behaves as an incompressible fluid; therefore, the specific internal energy of a system can be written as a function of the specific heat at constant volume and temperature, $\delta e_{int} \approx c_V \delta T$. For incompressible substances the specific heat at constant pressure and volume are identical $c_p \cong c_V$. The specific heats for the vapor are related by the gas constant $c_p = c_V + R_g$, assuming that the vapor behaves like an ideal gas. Heat crossing the control volume's boundaries is associated with the latent heat of evaporation and the energy associated with evaporation equals the latent heat multiplied with the mass that vaporizes, $\dot{m}_{lv,i} h_{fg,i}$. The expression for the energy conservation principle is simplified to a version in which the flow of energy is expressed in terms of the mass flow:

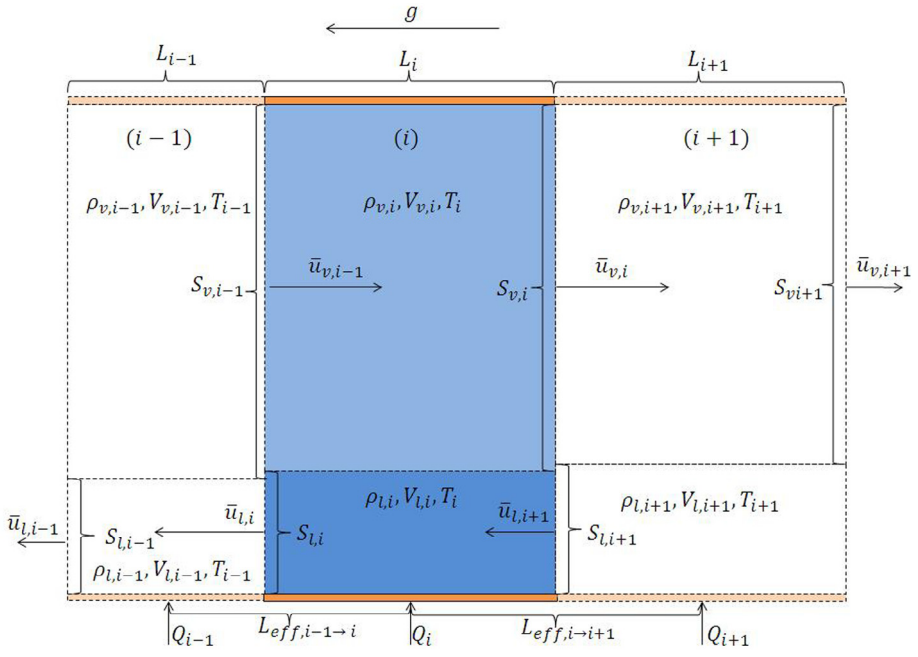

Fig. 4. Graphical representation of a control volume with its properties and flows used in the transient model.

Table 1
Relations between dimensions in a finite volume element.

Dimension	Relation	Dimension	Relation
$S_w=$	$2WL+2HL$	$V_{tot}=$	WHL
$S_v=$	$WH-S_l$	$V_v=$	$V_{tot}-V_l$
$h_v=$	$\sqrt{\frac{S_vH}{W}}$	$m_v=$	ρ_vV_v
$h_l=$	$\frac{H-h_v}{2}$	$w_v=$	$\frac{S_v}{h_v}$
$d_{h,l}=$	$\frac{4S_l}{2W+2H}$	$d_{h,v}=$	$\frac{4S_v}{2h_v+2w_v}$
$S_l=$	$\frac{V_l}{L}$		

$$\frac{d}{dt}((V_{l,i}\rho_{l,i}c_{V,l,i}+V_{v,i}\rho_{v,i}c_{V,v,i})T_i)+\dot{m}_{lv,i}h_{fg,i} = \rho_{v,i-1}S_{v,i-1}\bar{u}_{v,i-1}c_{p,v,i-1}T_{v,i-1}-\rho_{v,i}S_{v,i}\bar{u}_{v,i}c_{p,v}T_i + \rho_{l,i+1}S_{l,i+1}\bar{u}_{l,i+1}c_{p,l,i+1}T_{l,i+1}-\rho_{l,i}S_{l,i}\bar{u}_{l,i}c_{p,l}T_i+\dot{Q}_i \quad (6)$$

3.1.4. Conservation of momentum

The conservation of momentum focuses on the flow between two elements rather than the flow across the boundaries of one element. The momentum conservation equation can be adapted into the well-known Navier–Stokes equation. At low Mach numbers ($Ma \le 0.3$) incompressible flow can be assumed which leads to the following equation:

$$\rho\left(\frac{\partial \boldsymbol{u}}{\partial t}+\boldsymbol{u}\cdot\nabla\boldsymbol{u}\right)=-\nabla p+\mu\nabla^2\boldsymbol{u}+\rho\boldsymbol{f} \quad (7)$$

The inertia term depends on the time-dependent acceleration and the convective acceleration of the fluid. The convective acceleration component is disregarded due to the one-dimensional incompressible flow assumption. Gravity is the external body force acting on the volume. Only the change of momentum in the axial direction is taken into account and the velocity of the flow is taken uniform across the element. The pressure drop due to the viscous effects can be written as a pressure drop depending on a dimensionless friction factor fRe_h determined from an analytical relation. Assuming that downward liquid flow is positive, the Navier–Stokes equation can be rewritten for both the vapor and the liquid flows in a more usable form:

$$\rho_{l,i}\frac{d}{dt}(\bar{u}_{l,i})=-\frac{p_{l,i-1}-p_{l,i}}{L_{eff,i-1\to i}}-\frac{2(fRe_{h,l,i})\mu_{l,i}}{d^2_{h,l,i}}\bar{u}_{l,i}+\rho_{l,i}g \quad (8)$$

$$\rho_{v,i}\frac{d}{dt}(\bar{u}_{v,i})=-\frac{p_{v,i+1}-p_{v,i}}{L_{eff,i\to i+1}}-\frac{2(fRe_{h,v,i})\mu_{v,i}}{d^2_{h,v,i}}\bar{u}_{v,i}-\rho_{v,i}g \quad (9)$$

3.2. Analytical and empirical relations used in the numerical model

Wall temperatures and friction coefficients are determined using analytical and empirical relations from the literature. The following expressions are used in the described transient model.

3.2.1. Liquid friction factor

For the liquid friction factor $f_{Re_{h,l}}$ the definition of Schneider and DeVos [32] is used for the counter-current annular flow within the thermospyphon. Schneider and DeVos present a correlation based on a planar free liquid surface for various liquid cross sections (Eq. 10). Assuming that the thermosyphon has just one groove ($N=1$) with an overall film width of $w=2W+2H$ and with the height of the liquid film h_l, this equation is suitable for modeling a counter-current thermosyphon. The effects around the corners of the rectangular cross section are neglected.

$$f_{Re_{h,l}}=(f_{Re_{h,l}}0)\left(1+\frac{Nw^3}{6\pi d^3_{h,v}}(fRe_{h,v})\frac{\nu_v}{\nu_l}\left[1-1.971e^{\frac{-\pi h_l}{w}}\right]\right) \quad (10)$$

$$f_{Re_{h,l}}0=8h_l^2\left[\left(h_l+\frac{w}{2}\right)^2\left(\frac{1}{3}-\frac{32w}{\pi^5h_l}\tanh\frac{\pi h_l}{w}\right)\right]^{-1} \quad (11)$$

3.2.2. Vapor friction factor

In the case of steady state behavior, the liquid velocity will be a fraction of the vapor velocity due to the difference in density. Therefore at the liquid–vapor interface the liquid can be considered stationary. Shah and Bhatti [33] presented a friction factor for the vapor depending on the aspect ratio of the height and width of the vapor duct:

$$f_{Re_{h,v}}=24(1-1.3553\alpha+1.9467\alpha^2-1.7012\alpha^3+0.9564\alpha^4-0.2537\alpha^5) \quad (12)$$

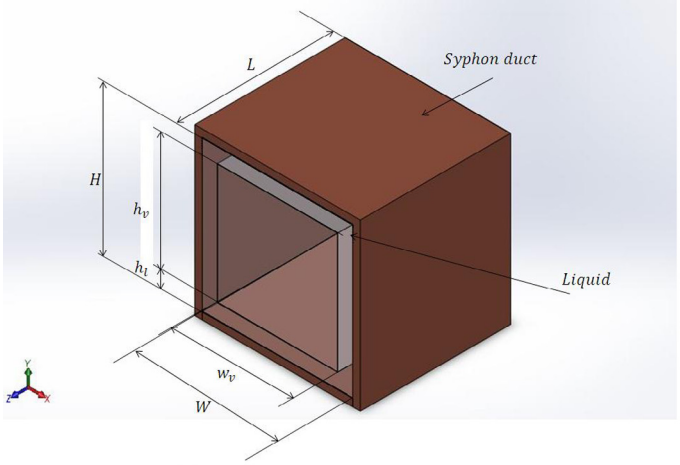

(a) basic finite volume element

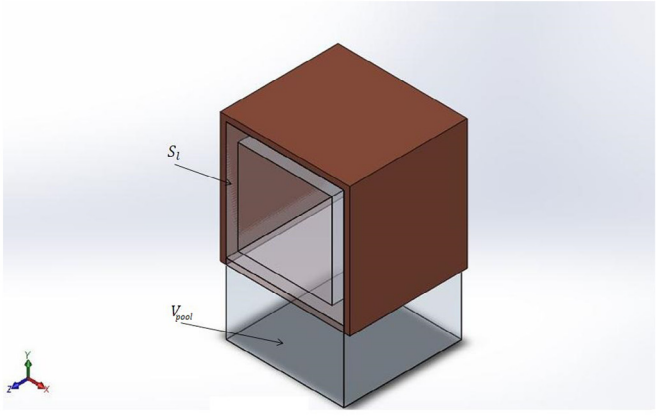

(b) finite volume element with cascading pool

Fig. 5. Control volume dimensions.

Table 2
Boundary conditions and model limitations.

Condition	Formulation	Limit or boundary conditions or limitation
1. Dry-out	$V_{l,i} = 0$	$\rho_{l,i}\frac{d}{dt}(\bar{u}_{l,i}) = 0$ and $\bar{u}_{l,i} = 0$
2. Pool is not filled	$V_{l,i} \leq V_{pool,i}$	$\rho_{l,i}\frac{d}{dt}(\bar{u}_{l,i}) = 0$ and $\bar{u}_{l,i} = 0$
3. Entirely filled with liquid	$V_{l,i} = V_{i,t}$ and $\bar{u}_{l,i+1} > 0$	Computational error
4. Evaporator end cap	–	$\rho_{l,i}\frac{d}{dt}(\bar{u}_{l,i}) = 0$ and $\bar{u}_{l,i} = 0$ and $\bar{u}_{v,i-1} = 0$
5. Condenser end cap	–	$\rho_{v,i}\frac{d}{dt}(\bar{u}_{v,i}) = 0$ and $\bar{u}_{v,i} = 0$ and

$$\alpha = \begin{cases} \frac{h_v}{w_v} & h_v < w_v \\ \frac{w_v}{h_v} & h_v > w_v \end{cases} \tag{13}$$

The friction factor of the vapor and liquid depends on the geometry of the cross section of the flow. The larger the hydraulic diameter, the less friction the flow will encounter. A vapor flow through a narrow rectangular duct with the same cross sectional area as a square duct will experience more friction according to Eq. (12). Hence, flattening decreases the performance of the thermosyphon. It is therefore that the width and height of the cross section are taken equal in the proposed design, resulting in a vapor friction factor $f_{Re_{h,v}} \approx 14$.

3.2.3. Wall temperatures

A lumped approach for the vapor and liquid temperatures inside the control volume is used. For the determination of the wall temperatures of a specific control volume element, the type of this element needs to be known as different expressions can be used for modeling different conditions, such as pool boiling or film condensation.

For a condenser element classical Nusselt theory is adopted [23] for modeling film condensation along the thermosyphon's wall. The wall temperature $T_{w,c}$ of the element is expressed by Eq. (14) as a function of the liquid height h_l using the element temperature T_i as the saturation temperature. Finally, the heat rate leaving the condenser element is related to the wall temperature (Eq. 15). It is dependent on the thermal resistance of the cooler R_c and the ambient temperature T_{amb}.

$$T_{w,c} = T_i - \frac{h_l^4 \rho_l (\rho_l - \rho_v) g h_{fg}}{4 k_l \mu_l L} \tag{14}$$

$$\dot{Q}_{out} = -\frac{T_{w,c} - T_{amb}}{R_c} \tag{15}$$

The dependence on the liquid height is less convenient for determining the wall temperature in the evaporator because of the cascading elements. The heat transfer coefficient by Imura et al. [19] is therefore adopted (Eq. 16). The advantage of using this empirical heat transfer correlation is the independence of the liquid position in the element. This correlation is valid for nucleate boiling and overestimates the heat transfer coefficient during natural convection boiling and regular evaporation. The determination of the wall temperature at the evaporator section $T_{w,e}$ is computed by Eq. (17) using the temperature in the finite volume T_i. Here, the area of heat transfer S_w is estimated to be equal to the total contact area between the wall and liquid.

$$\bar{h}_e = 0.32 \left(\frac{\rho_l^{0.65} k_l^{0.3} c_{p,l}^{0.7} g^{0.2} \left(\frac{\dot{Q}_{in}}{S_w} \right)^{0.4}}{\rho_v^{0.25} h_{fg}^{0.4} \mu_l^{0.1}} \right) \left(\frac{p_{sat}}{p_{atm}} \right)^{0.3} \tag{16}$$

$$T_{w,e} = \frac{\dot{Q}_{in}}{S_w \bar{h}_e} + T_i \tag{17}$$

3.3. Implementation of boundary conditions and model limitations

Table 2 shows the boundary conditions and different limitations that apply to the model. The implementation can be described as follows:

1. **Dry-out** – In the case of dry-out of the evaporator end cap ($V_{l,i} = 0$), the liquid velocity, the liquid mass and liquid net rate of change of momentum will be zero.
2. **Pool is not filled** – In the case that an element has a liquid pool with volume V_{pool} which has not been entirely filled with liquid, no liquid can flow through (i.e. no overflowing), meaning the liquid velocity leaving the element is zero.
3. **Entirely filled with liquid** – When an element is entirely filled with liquid, numerical issues start to arise because the cross sectional area of the vapor becomes zero and no vapor can leave the element. This implies also that the minimum finite volume element size is bounded. A computational error is given when no numerical solution can be found and either the element size needs to be increased or the amount of working fluid need to be adjusted.
4. **Evaporator end cap** – At the evaporator end cap no fluid should leave the system. To account for this in the model, no energy, momentum and mass can cross that boundary.
5. **Condenser end cap** – At the condenser end cap no fluid should leave the system. To account for this in the model, no energy, momentum and mass can cross that boundary.

3.4. Model setup

The model is used to determine the effects on geometric changes and the effect of the cascading pools on the liquid mass flow. Important scenario parameters such as the geometry, ambient temperature, heat rate and condenser resistance can be adjusted. The entire experimental design is modeled using multiple elements. Each finite volume element performs a specific role. It is either modeled as a condenser element, an adiabatic element, an evaporator element or a cascading pool (i.e. an evaporator element with the additional buffer volume V_{pool}). The specific sequence of these elements resembles the entire thermosyphon design. In order to compare the modeled results with the experimental data a

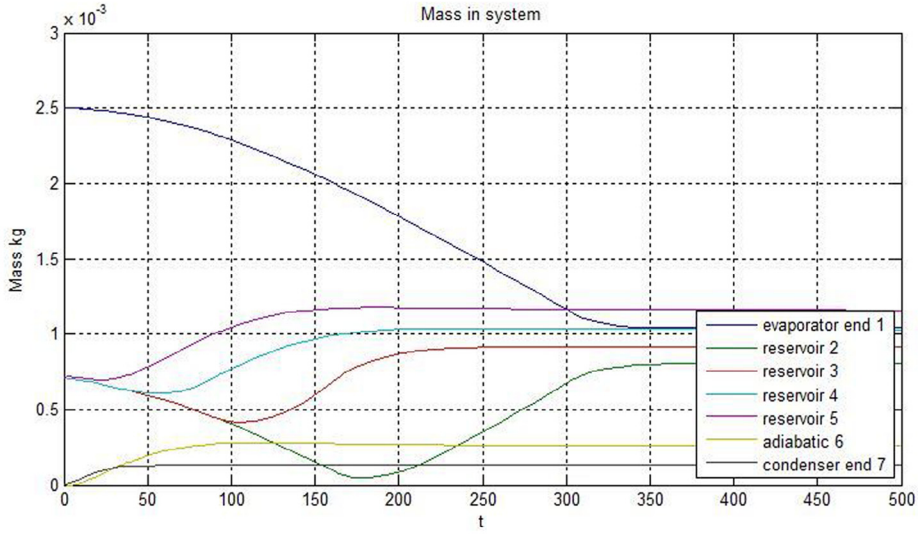

(a) liquid mass residing in the control volumes

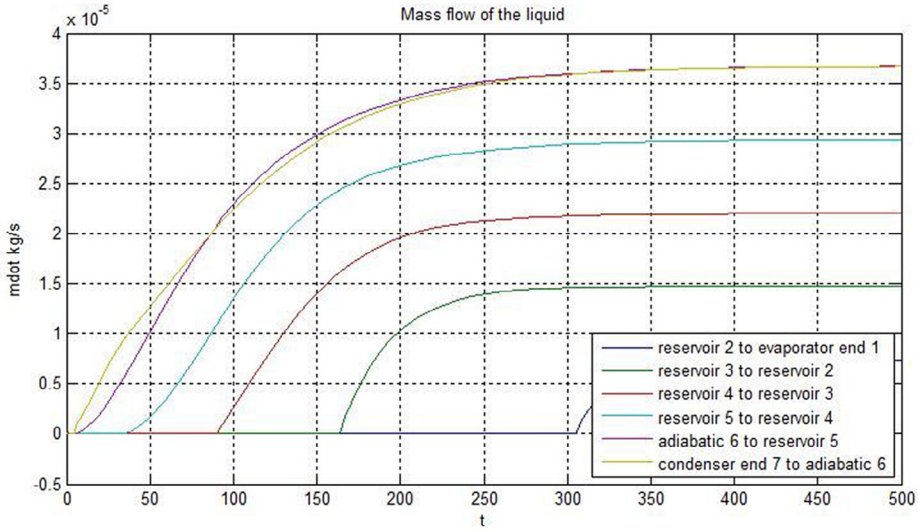

(b) liquid mass flow through the control volumes

Fig. 6. Transient model results for the 80 W power input. (For interpretation of the references to color in this figure legend, the reader is referred to the web version of this article.)

sequence of seven elements was created. The entire evaporator section was split into five elements: four cascading finite elements (reservoir elements) and one evaporator end cap element. Each having a length of 60 mm interpolated from the experimental design. The adiabatic section and the condenser section of the design were both modeled with one element each. The elements' properties, like the duct width W and height H, are modeled after the experimental design.

The model was used to determine the minimum required liquid fill ratio in the thermosyphon to overcome dry-out in the evaporator end cap and the cascading pools. The cascading finite elements in the model may contain up to 7.2 ml of liquid fluid.

The mass residence over time within the control volume elements is shown in Fig. 6a. Here, the input power $\dot{Q}_{in}$ is assumed to be 80 W spread evenly across the entire length of the evaporator section. At the start of the simulation the cascading pools are assumed to be filled and an excess fluid charge of 25 ml resides in the evaporator end cap. The simulation demonstrates that for these settings, the fluid charge of the lowest reservoir (Reservoir 2) is critical before reaching a steady state operation. The minimum size a cascading pool needs to have to prevent dry-out is mainly determined by the total number of pools and could be further optimized using a variable pool size along the evaporator length. Fig. 6b shows the liquid mass leaving a control volume element over time. The critical point of Reservoir 2 is overcome when Reservoir 3 starts overflowing at around 170 s.

Both figures also demonstrate the delay between inflow and outflow when cascading pools first overflow. For instance, around 310 s (Fig. 6a) liquid starts to flow from Reservoir 2 to the evaporator end cap. However, the liquid mass residing in the evaporator end cap still decreases, as the amount of mass evaporating and leaving the control volume exceeds the inflow. An equilibrium between the liquid mass inflow and vapor mass outflow is, in this case, reached around 330 s (Fig. 6b) about 20 s later. Similar behavior and results were found for different heat rates.

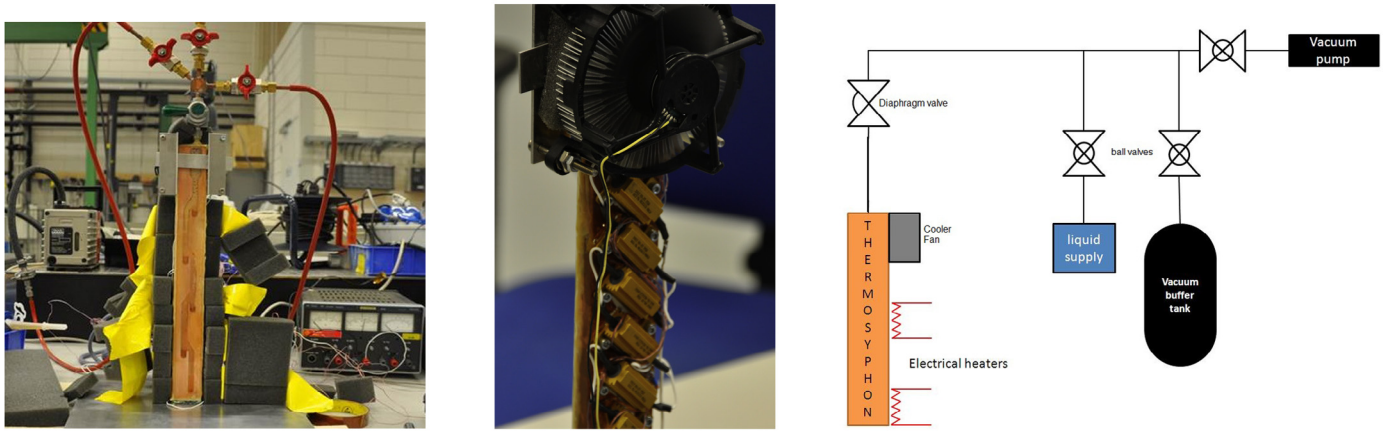

(a) photograph of the test rig

(b) electrical heaters on the back of the thermosyphon

(c) schematic setup of the test rig

Fig. 7. Experimental setup of the thermosyphon with cascading pools.

In general, the simulation results were found to be similar to the theoretical mass flow at steady state that should exist in the adiabatic section (Eq. 18). The temperature predictions of the model are presented in Section 5 along with the experimental data. The comparison between the model and the experimental data is further discussed in Section 6.3.

$$\dot{m}_{ss} = \frac{\dot{Q}_{in}}{h_{fg}} \tag{18}$$

4. Experimental test procedure

To experimentally validate the thermosyphon with cascading pools, shown in Fig. 7a, a heat load is applied using twelve evenly spread electrical resistors (Dale RH-25 25W 56Ω1%) (Fig. 7b). At the top of the thermosyphon a fan based cooler (Intel E97379-001) is clamped using brackets. The thermal resistance of the fan including the brackets was determined experimentally to be 0.39 K/W. At the base of the thermosyphon a block of insulation material is placed between the bottom plate and the thermosyphon to reduce the amount of heat that is transferred from the thermosyphon to the surroundings through the bottom.

Twelve T-type thermocouples, having an accuracy of 1 °C, are placed on the back of the thermosyphon. Six thermocouples evenly spread across the evaporator section, one in the adiabatic section and 3 evenly spread across the condenser section. The position of each thermocouple was already indicated in Fig. 2. Two other thermocouples were used to measure the ambient temperature. The ambient temperature is measured to determine the effect of changes in ambient temperature on the thermosyphon behavior using a climate chamber. All thermocouples are connected to a data logger that records one measurement every five seconds. The entire thermosyphon was packed in a 20 mm thick polymeric foam to prevent heat loss due to natural convection.

A vacuum buffer tank was used in the test rig to evacuate non-condensible gases without damaging the vacuum pump. A schematic overview of the test rig is shown in Fig. 7c. Water was chosen as the working fluid for ease of handling and safety reasons. Filling was done by boiling the working fluid first to get rid of most of the non-condensible gases. It was then supplied to the thermosyphon, which was preheated and evacuated. The thermosyphon was connected to the buffer tank and heat was supplied until the desired fill ratio was reached and the remaining non-condensible gases were extracted.

A camera was placed in front of the thermosyphon to record the behavior of the evaporator and condenser at steady state. This was done after temperature measurements were taken and the insulation material near the glass cover was locally removed. The measurements that were taken started with a uniform temperature inside the entire thermosyphon at ambient temperature. After the fan was turned on, the data logger began recording. Simultaneously with the start of the recording, the power supply for the electrical heaters was turned on. The power supplied was matched with the desired heat rate to be dissipated. An experiment lasted until or beyond a continuous steady state was reached and temperatures differed only little in comparison to the time scale (i.e. 60 s/K integrated over 10 measurements). An experiment was aborted earlier if thermosyphon limitations, such as dry-out, were experienced.

5. Experimental validation

5.1. Analysis of the transient behavior

The transient behavior at 40 W of input power is shown in Fig. 8. The experimental data are represented by the solid lines and the thermocouple number and location correspond with the numbering and location as presented in Fig. 2. The thick dashed lines represent the simulated wall temperature of the evaporator end cap, adiabatic section and the condenser end cap. The maximum temperature difference across the thermosyphon is indicated by the dash-dotted red line. The transient behavior of the measurements shows a graduate increase in temperature along the thermosyphon. Steady state was reached after about half an hour for most of the experimental runs. Similar behavior was found for other power inputs.

The transient model reaches steady state at an earlier state. The simulated wall temperatures show good agreement with the lower evaporator temperatures for all experimental runs. The temperature gradient in the evaporator section of the experimental data is not present in the results of the numerical model. The model shows similar results for all evaporator elements due to the fact that temperatures are computed using the saturation temperature (Eq. 16). Good agreement is found with the temperatures in the condenser section using the classical Nusselt film layer theory (Eq. 14).

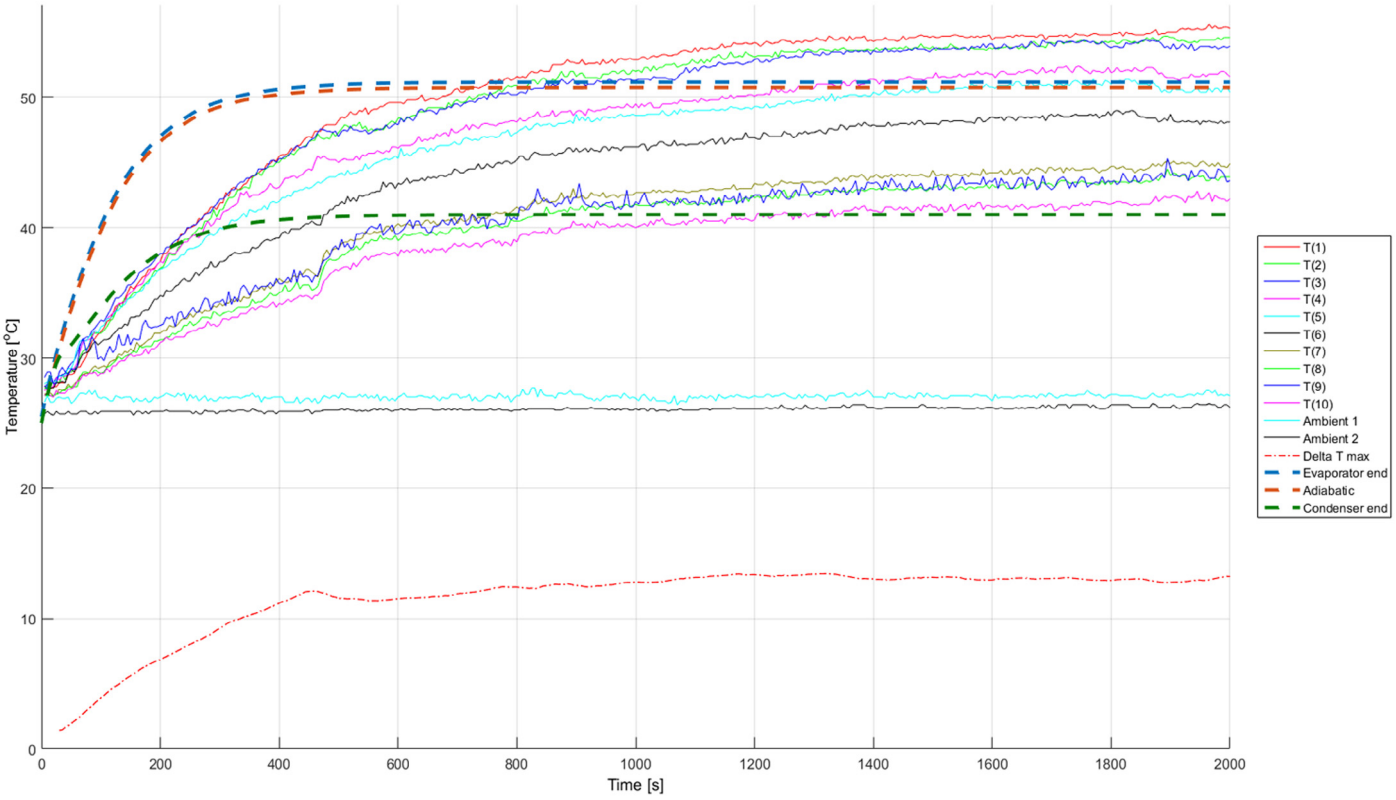

Fig. 8. Transient analysis for the 40 W power input; measured (solid) and simulated (dashed) results. (For interpretation of the references to color in this figure legend, the reader is referred to the web version of this article.)

5.2. Ambient temperature influence

The influence of the ambient temperature on the thermosyphon's performance was tested as well. Fig. 9 shows the influence of adjusting the ambient temperature using a climate chamber for an 80 W run. The adjusted ambient temperature influences the temperature of the condenser and hence the entire thermosypon, leading to different thermosyphon behaviors. Measurements were carried out in a climate chamber with temperatures ranging from 5 °C to about 45 °C. This temperature is depicted by light-blue (cyan) solid line, denoted as climate chamber. Note that in this measurement the black solid line, denoted ambient, represents the ambient temperature outside the climate chamber.

The results demonstrate that the performance stabilizes with a rising ambient temperature as the maximum temperature difference, indicated by the dash-dotted red line, in the thermosyphon is maintained. The maximum temperature difference is similar to the results measured for an 80 W run at room temperature without climate chamber.

Fig. 9 also shows that, as can be predicted, the thermophysical properties of working fluid influence the thermal performance negatively at lower temperatures, as the maximum temperature difference is a bit higher here.

5.3. Overall thermal performance

The overall performance of the thermosyphon with cascading pools is evaluated during steady state behavior. The performance is specified by the thermal resistance found at a specific operating temperature and heat rate, according to Eq. (19).

$$R_{thermosyphon} = \frac{T_{max} - T_{min}}{\dot{Q}_{in}} \tag{19}$$

This is under the assumption that no heat is lost through the insulating material. The performance values are listed in Table 3. The predicted performances from the transient model are given as well. As mentioned the temperature gradient in the evaporator is not captured by the model, which is the major cause for the difference in the listed results. The experimental results indicate that the thermal performance increases for higher heat rates. The average temperature difference across the entire evaporator $\Delta T_{evaporator_{max}}$ during all runs is measured to be ≈9 K, with the exception of the 80 W run. This is caused by the behavior of the second pool upward from the evaporator end cap and will be discussed in Section 6.1.

5.4. Temperature distribution analysis

A temperature distribution analysis is depicted in Fig. 10. It is used for the evaluation of the evaporator temperature at steady state. The wall temperatures are shown at various positions on the thermosyphon for different heat rates and at different ambient temperatures, e.g. the 60–27 line indicates a heat rate of 60 W and an ambient temperature of 27 °C. The temperatures shown in this figure are the average of the last 10 measurements in order to filter measurement noise. The temperature distribution for various heat rates shows an overall graduate linear decrease in temperature from the middle of the evaporator toward the condenser section for all heat rates. Variations in this generic profile are found near the condenser end cap and close to the evaporator end cap.

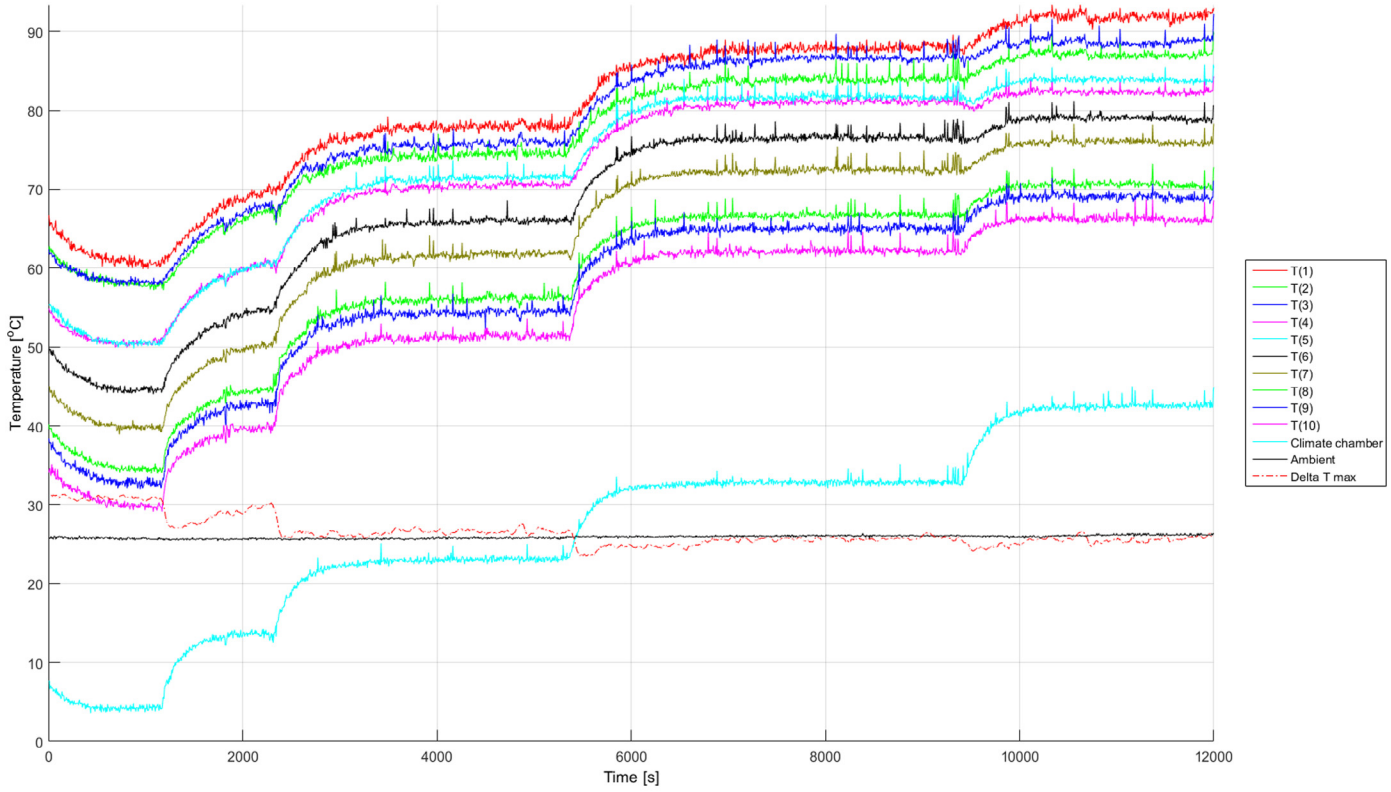

Fig. 9. Transient analysis for the 80 W power input within a climate chamber environment. (For interpretation of the references to color in this figure legend, the reader is referred to the web version of this article.)

Table 3
Steady state values from the experimental data, at ≈27 °C ambient temperature.

$\dot{Q}_{in}$ (W)	T_{amb} (°C)	ΔT_{max} (K)	$\Delta T_{evaporator_{max}}$ (K)	R_{max} (K/W)	$R_{predicted}$ (K/W)
100	27	23.6	9.9	0.24	0.13
90	26	21.4	9.0	0.24	0.14
80	27	21.9	12.6	0.27	0.16
70	27	17.9	7.9	0.26	0.19
60	27	17.8	9.7	0.30	0.22
40	27	14.4	8.2	0.36	0.25

As the vapor mass flow travels toward the condenser, the decrease in temperature tends to progress. This is partly due to the increasing vapor mass flow and thus increasing friction. As the vapor flows toward the condenser, the evaporated mass from all cascading pools is accumulated. Also, the vapor flow traveling upward through the adiabatic section still has an interaction with the cooler condensate that is flowing down. As liquid fluid flows back toward the evaporator section it gradually heats up. This is caused by locally condensing vapor and heat leakage from the evaporator section

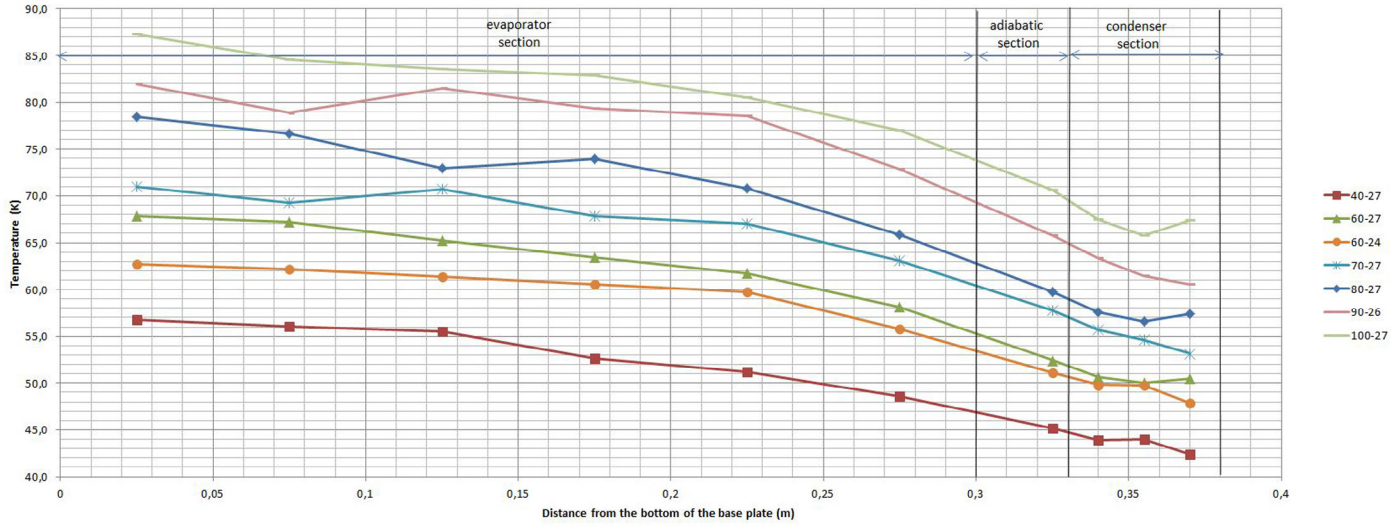

Fig. 10. Temperature distribution analysis for various power inputs and ambient temperatures. (For interpretation of the references to color in this figure legend, the reader is referred to the web version of this article.)

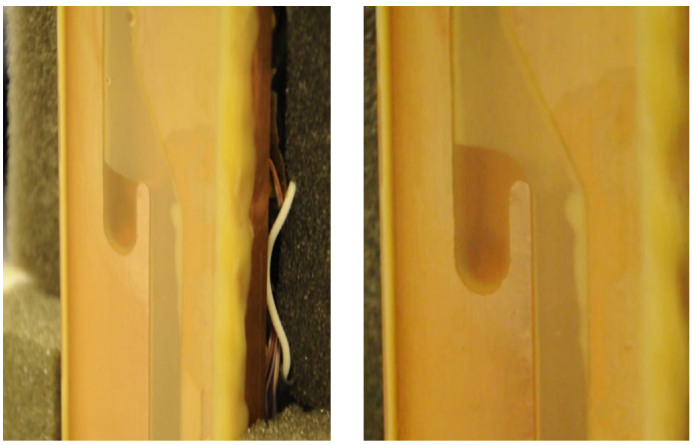

(a) pool at 60W run (c) pool at 100W run

Fig. 11. Visualization of a single cascading pool.

toward the adiabatic section, both causing a temperature gradient in both the condenser and adiabatic sections. The amount of heat leakage by conduction from the evaporator section toward the adiabatic section has been minimized by the local removal of copper material at the back of the thermosyphon, resulting in a local wall thickness of 1 mm of the copper profile. The temperature gradient in the adiabatic section is minimally affected by an overall increase in heat rate.

6. Discussion

6.1. Interpretation of the observed experimental data

Natural convection boiling and nucleate boiling in the pools were observed in all experiments for most of the liquid pools. Fig. 6 shows one of the cascading pools for a 60 W and 100 W run. The difference in boiling regimes is caused by the relatively low radial heat flux, leading to a small temperature difference between the liquid and wall. This low temperature difference prevents nucleate boiling from occurring. Smooth surfaces caused by the milling process prevent the initiation of nucleates as well, causing rapid bursts of liquid whenever a nucleate comes into existence. This geyser effect is experienced in the evaporator end cap showing rapid bubble formations and growth, which rapidly expels the liquid upward into the thermosyphon. Upon contact with the wall, part of the expelled liquid instantly evaporates, locally creating a cooling effect at the thermosyphon wall. This causes minor fluctuation in the wall temperature.

Small differences in fill ratio of the evaporator end cap are influencing the geyser phenomenon. The amount of liquid in the evaporator end cap determines the type of boiling to be experienced. Increasing the liquid amount in the pool promoted nucleate boiling and eventually led to geyser boiling. Natural convection boiling and nucleate boiling are more stable processes, although a pulsating effect can be achieved with geyser boiling. Geyser boiling rewets the wall around the pool at the expense of increased frictional effects due to turbulent and unpredictable flow patterns.

At increased heat rates, an increase in mass flow is present, causing the higher situated pools to contain more liquid. This is shown in Fig. 11c. The extra amount of liquid contained in the thermosyphon pools varied over a large time period, caused by droplets of liquid that condense on the glass surface and migrated downward. An increase in liquid mass in the cascading pool was also experienced in the experiments. Surface tension forces cause the liquid to retract to the corners of the rectangular profile, instead

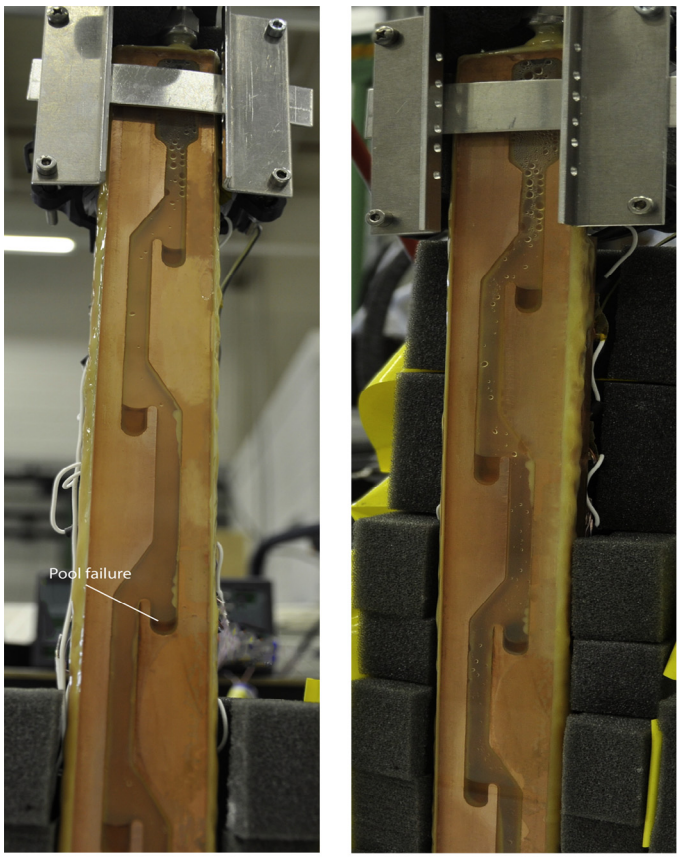

(a) pool failure at heat rates of $70 - 90\ W$ (b) proper pool functioning at higher heat rates ($100\ W$)

Fig. 12. Visualization of the thermosyphon with cascading pools in operation.

of forming an equally spread film on all copper sides. The retracted liquid resulted in dry spots in the evaporator section, resulting in a smaller heat transfer area.

Most of the pools functioned as designed; liquid filled and overflowed over the edge and was carried downward. Liquid accumulated in the pools before overflowing occurred. Because of poor adhesion of the glass top to the copper bar, one pool showed a different behavior. The second pool upward from the evaporator end cap did not function properly due to an intern capillary groove that carried the liquid down to the evaporator end cap. Visual data showed that reentering liquid from that capillary groove evaporated instantly.

6.2. Interpretation of the temperature distribution

A linear decreasing temperature gradient near the evaporator end cap is not obtained at heat rates of 70–90 W. It was observed that temperatures near the second pool upward from the evaporator end cap deviated from the linear temperature profile at increased heat rates. This is a consequence of the poor liquid accumulation in this pool and reentry of the superheated liquid below this pool into the system near the evaporator end cap. This is shown in Fig. 12a. This case is interesting from an engineering perspective as its shows the robustness of the system. Would there exist such a production defect the thermosyphon is still capable to operate. A further increase of the heat flux demises the effect as liquid starts to accumulate again in the cascading pool, as shown in Fig. 12b. The mass flow through the capillary is in that case lower than the liquid mass flow into the pool. The effect on the temperature gradient is not noticeable at low heat rates.

Temperature differences near the condenser end cap can be explained by the presence of non-condensible gases that could not be totally removed. They influence the temperature readings at the condenser end cap. Diffused gases in the liquid after filling and the diffusion of gases through the adhesive over time are a cause for their presence.

6.3. Discussion on the numerical model

The model reaches steady state earlier than the experimental design. The explanation is the exclusion of the thermal mass of the insulating material, glass cover and electrical resistors in the model. One explanation for the relative small temperature difference in the evaporator section is that the pressure difference due to frictional effects on the vapor is underestimated. One cause is that frictional effects of the bends in the thermosyphon are not taken into account in the model. An accurate estimation for the wall temperature in the evaporator section is proven difficult in the current setup due to the influence of the actual heat transfer area in the model segments, the glass surface and the unpredictable transition between boiling regimes. The use of various other empirical heat transfer coefficient correlations from the discussed literature, including other boiling regimes, did not generate more accurate results. Hence, modeling heat transfer characteristics in the evaporator needs further investigation.

6.4. Discussion on the prototype design

Investigating the pressure drop inside the thermosyphon and focusing on the heat transfer mechanism and coefficients in the evaporator is needed for more accurate wall temperature estimations. The experimental results confirm the working principle of this type of thermosyphon using the principle of cascading pools. The test results demonstrate the promising potential to implement such design features in thermosyphons. The current performance can be enhanced by optimizing the cascading pool design and the changing the glass plate for a metal cover.

7. Conclusion

A novel design for integrating a two-phase closed thermosyphon with cascading pools into a planer sheet of metal has been proposed. The design focuses on establishing a low-temperature gradient for a long evaporator section while having a short condenser section. Innovative design features include the new layout, consisting of multiple evaporator pools cascaded along the length of the thermosyphon. A numerical model based on finite volume elements is presented. A test prototype and experimental setup was build. Experiments have been carried out and compared with the model to prove the working principle of this new type of thermosyphon. The current numerical model is able to capture the effect of overflowing cascaded pools and properly predict the transient behavior of the mass flow. The temperature gradient in the evaporator section is however underpredicted. The promising experimental results prove the working principle of this innovative design.

Acknowledgement

The authors would like to thank Thales Nederland B.V. for the support and available equipment for testing the thermosyphon's design and operation.

Appendix: Supplementary material

Supplementary data to this article can be found online at doi:10.1016/j.applthermaleng.2015.12.095.

Nomenclature

c_p	Specific heat at constant pressure (J kg^{-1} K^{-1})
c_V	Specific heat at constant volume (J kg^{-1} K^{-1})
D	Diameter (m)
D_h	Hydraulic diameter (m)
E	Energy (J)
f	Force vector (N)
$\mathbf{f}$	Friction coefficient (–)
g	Gravitational constant (m s^{-2})
H	Height (m)
h	Heat transfer coefficient (W m^{-2} K^{-1})
h_l	Height of the liquid film (m)
h_v	Height of the vapor duct (m)
h_{fg}	Latent heat of evaporation (J kg^{-1})
k	Thermal conductivity (W m^{-1} K^{-1})
L	Length (m)
m	Mass (kg)
$\dot{m}$	Mass flow (kg s^{-1})
Ma	Mach number (–)
$\mathbf{n}$	Normal vector (–)
p	Pressure (N m^{-2})
Q	Heat (J)
$\dot{Q}$	Heat rate (W)
$\dot{q}$	Heat flux (W m^{-2})
R	Thermal resistance (W K^{-1})
Re	Reynolds number (–)
S	Surface or Area (m^2)
t	Time (s)
T	Temperature (K)
u	Velocity (m s^{-1})
V	Volume (m^3)
W	Width of the thermosyphon (m)
W	Work (J)
w_v	Width of the vapor duct (m)
α	Width height ratio (–)
ρ	Density (kg m^{-3})
Δ	Increment (–)
μ	Dynamic viscosity (kg m^{-1} s^{-1})
ν	Kinematic viscosity (m^2 s^{-1})
τ	Shear stress (N m^{-2})

Subscripts

Symbol	Description
a	Adiabatic
atm	Atmosphere
c	Condenser
e	Evaporator
eff	Effective
int	Internal
i	Index i
in	In flow
l	Liquid
out	Out flow
pool	Cascading pool
rel	Relative
sat	Saturation
tot	Total
v	Vapor
V	Volume
w	Wall

References

[1] Z. Zuo, F. Gunnersons, Numerical modeling of the steady-state two-phase closed thermosyphon, Int. J. Heat Mass Transf. 37 (17) (1994) 2715–2722,

doi:10.1016/0017-9310(94)90388-3 <http://www.sciencedirect.com/science/article/pii/0017931094903883>.
[2] D. Reay, P. Kew, R. McGlen, Heat Pipes, Butterworth-Heinemann, Oxford, 2006.
[3] C. Vincent, J. Kok, Investigation of the overall transient performance of the industrial two-phase closed loop thermosyphon, Int. J. Heat Mass Transf. 35 (6) (1992) 1419–1426 <http://doc.utwente.nl/32248/>.
[4] B. Jiao, L. Qiu, X. Zhang, Y. Zhang, Investigation on the effect of filling ratio on the steady-state heat transfer performance of a vertical two-phase closed thermosyphon, Appl. Therm. Eng. 28 (11–12) (2008) 1417–1426, doi:10.1016/j.applthermaleng.2007.09.009 <http://linkinghub.elsevier.com/retrieve/pii/S1359431107003122>.
[5] J. Perkins, UK Patent No. 7059, 1836.
[6] H. Cohen, F. Bayley, Heat transfer problems of liquid cooled gas-turbine blades, Proc. IMechE 169 (1955) 1068–1080.
[7] A. Alizadehdakhel, M. Rahimi, A. Alsairafi, Cfd modeling of flow and heat transfer in a thermosyphon, Int. Commun. Heat Mass 37 (3) (2010) 312–318, doi:10.1016/j.icheatmasstransfer.2009.09.002 <http://linkinghub.elsevier.com/retrieve/pii/S0735193309002188>.
[8] R. Sakhuja, Flooding constraint in wickless heat pipes, ASME Publ. Paper No. 73-WA/HT-7, 1973.
[9] Y. Katto, Generalized correlation for critical heat flux of the natural convection boiling in confined channels, Trans. Jpn. Soc. Mech. Eng. 44 (1978) 3908–3911.
[10] C. Tien, K. Chung, Entrainment limits in heat pipes, AIAA J. 17 (1979) 643–646.
[11] H. Nguyen-Chi, M. Groll, Entrainment or flooding limit in a closed two-phase thermosyphon, in: Proc. 4th Int. Heat Pipe Conf., Tsukuba, Japan, 1981, pp. 147–162.
[12] A. Faghri, Heat Pipe Science and Technology, 1st ed., Taylor & Francis, New York, 1995.
[13] A. Streltsov, Theoretical and experimental investigation of optimum filling for heat pipes, Heat Transfer Sov. Res. 7 (1975) 23–27.
[14] M. Shiraishi, M. Yoneya, A. Yabe, Visual study of operating limit in the two-phase thermosyphon, in: Proc. 5th Int. Heat Pipe Conf., 1984, pp. 11–17.
[15] Z. Gorbis, G. Savchenkov, Low temperature two-phase closed thermosyphon investigation, in: Proc. 2th Int. Heat Pipe Conf., 1984, pp. 37–45.
[16] M. Bezrodny, Fundamental questions of closed two-phase thermosyphons, in: L. Vasiliev, S. Kaka (Eds.), Heat Pipes and Solid Sorption Transformations, CRC Press, 2013, pp. 319–356, doi:10.1201/b14864-10.
[17] H. Imura, K. Sasaguchi, H. Kozai, S. Numata, Critical heat flux in a closed two-phase thermosyphon, Int. J. Heat Mass Transf. 26 (8) (1983) 1181–1188, doi:10.1016/S0017-9310(83)80172-0 <http://linkinghub.elsevier.com/retrieve/pii/S0017931083801720>.
[18] Y. Park, H. Kang, C. Kim, Heat transfer characteristics of a two-phase closed thermosyphon to the fill charge ratio, Int. J. Heat Mass Transf. 45 (23) (2002) 4655–4661, doi:10.1016/S0017-9310(02)00169-2 <http://linkinghub.elsevier.com/retrieve/pii/S0017931002001692>.
[19] H. Imura, H. Kusuda, J. Ogata, T. Miyazaki, N. Skamoto, Heat transfer in two-phase closed-type thermosyphons, Trans. Jpn. Soc. Mech. Eng. Series B (1979) 712–722.
[20] C. Casarosa, E. Latrofa, A. Shelginski, The geyser effect in a two-phase thermosyphon, Int. J. Heat Mass Transf. 26 (6) (1983) 933–941, doi:10.1016/S0017-9310(83)80117-3 <http://linkinghub.elsevier.com/retrieve/pii/S0017931083801173>.
[21] T. Kiatsiriroat, A. Nuntaphan, J. Tiansuwan, Thermal performance enhancement of thermosyphon heat pipe with binary working fluids, Exp. Heat Transfer 13 (2000) 137–152.
[22] W. Rohsenow, Heat transfer and temperature distribution in laminar film condensation, Trans. ASME 78 (1956) 1645–1648.
[23] W. Nusselt, Die oberflachenkondensation des wasserdampfes, Z. Ver. Dtsch. Ing. 60 (1916) 541–546, 569–575.
[24] S. Kutateladze, Fundamentals of Heat Transfer, 1963.
[25] W.W. Wits, J.B. Kok, Modeling and validating the transient behavior of flat miniature heat pipes manufactured in multilayer printed circuit board technology, J. Heat Transfer 133 (8) (2011) doi:10.1115/1.4003709.
[26] W. Srimuang, S. Rittidech, B. Bubphachot, Heat transfer characteristics of a vertical flat thermosyphon, J. Mech. Sci. Technol. 23 (2009) 2548–2554, doi:10.1007/s12206-009-0703-.
[27] P. Amatachaya, W. Srimuang, Comparative heat transfer characteristics of a flat two-phase closed thermosyphon (ftpct) and a conventional two-phase closed thermosyphon (ctpct), Int. Commun. Heat Mass 37 (3) (2010) 293–298, doi:10.1016/j.icheatmasstransfer.2009.11.004 <http://linkinghub.elsevier.com/retrieve/pii/S0735193309002656>.
[28] M. Zhang, Z. Liu, G. Ma, The experimental investigation on thermal performance of a flat two-phase thermosyphon, Int. J. Therm. Sci. 47 (9) (2008) 1195–1203, doi:10.1016/j.ijthermalsci.2007.10.004 <http://linkinghub.elsevier.com/retrieve/pii/S1290072907002153>.
[29] J. Lee, J. Ko, Y. Kim, S. Jeong, T. Sung, Y. Han, et al., Experimental study on the double-evaporator thermosiphon for cooling hts (high temperature superconductor) system, Cryogenics 49 (8) (2009) 390–397, doi:10.1016/j.cryogenics.2009.04.004 <http://linkinghub.elsevier.com/retrieve/pii/S0011227509000654>.
[30] Y. Cengel, Heat and Mass Transfer, third ed., McGraw-Hill, 2006.
[31] D. Wilcox, Basic Fluid Mechanics, fifth ed., DCW Industries, 2012.
[32] G. Schneider, R. DeVos, Nondimensional analysis for the heat transport capability of axially-grooved heat pipes including liquid/vapor interaction, in: Proceedings of the 18th AIAA Aerospace Sciences Meeting, 1980.
[33] R. Shah, M. Bhatti, Laminar convective heat transfer in ducts, in: Handbook of Single-Phase Convective Heat Transfer, John Wiley & Sons, 1987.